



UNIVERSITY OF LEEDS

This is a repository copy of *Sensing, measuring and modelling the mechanical properties of sandstone*.

White Rose Research Online URL for this paper:
<http://eprints.whiterose.ac.uk/122676/>

Version: Accepted Version

Article:

Antony, SJ orcid.org/0000-0003-1761-6306, Olugbenga, A and Ozerkan, N (2018) Sensing, measuring and modelling the mechanical properties of sandstone. *Rock Mechanics and Rock Engineering*, 51 (2). pp. 451-464. ISSN 0723-2632

<https://doi.org/10.1007/s00603-017-1347-3>

© Springer-Verlag GmbH Austria 2017. This is an author produced version of a paper published in *Rock Mechanics and Rock Engineering*. Uploaded in accordance with the publisher's self-archiving policy.

Reuse

Items deposited in White Rose Research Online are protected by copyright, with all rights reserved unless indicated otherwise. They may be downloaded and/or printed for private study, or other acts as permitted by national copyright laws. The publisher or other rights holders may allow further reproduction and re-use of the full text version. This is indicated by the licence information on the White Rose Research Online record for the item.

Takedown

If you consider content in White Rose Research Online to be in breach of UK law, please notify us by emailing eprints@whiterose.ac.uk including the URL of the record and the reason for the withdrawal request.



eprints@whiterose.ac.uk
<https://eprints.whiterose.ac.uk/>

Sensing, measuring and modelling the mechanical properties of sandstone

S. J. Antony*¹, A. Olugbenga¹ and N.G. Ozerkan²

¹ School of Chemical and Process Engineering, University of Leeds, LS2 9JT, UK

² Center for Advanced Materials, P. O. Box: 2713 Qatar University, Qatar

* Corresponding author: S.J.Antony@leeds.ac.uk

ABSTRACT

We present a hybrid framework for simulating the strength and dilation characteristics of sandstone. Where possible, the grain-scale properties of sandstone are evaluated experimentally in detail. Also, using photo-stress analysis, we sense the deviator stress (σ/ϵ) distribution at the microscale and its components along the orthogonal directions on the surface of a V-notch sandstone sample under mechanical loading. Based on this measurement and applying a grain-scale model, the optical anisotropy index K_0 is inferred at the grain scale. This correlated well with the grain contact stiffness ratio K evaluated using ultrasound sensors independently. Thereafter, in addition to other experimentally characterised structural and grain-scale properties of sandstone, K is fed as an input into the discrete element modelling of fracture strength and dilation of the sandstone samples. Physical bulk scale experiments are also conducted to evaluate the load-displacement relation, dilation and bulk fracture strength characteristics of sandstone samples under compression and shear. A good level of agreement is obtained between the results of the simulations and experiments. The current generic framework could be applied to understand the internal and bulk mechanical properties of such complex opaque and heterogeneous materials more realistically in future.

Key words: Micromechanics, rock mechanics, mechanical properties, optical stress analysis, DEM

1. INTRODUCTION

Fundamental level understandings on the strength and fracture properties of opaque and heterogeneous materials such as sandstone rock require accounting for realistic characteristics, from the single-grain scale to the bulk scale. This task remains as a stiff challenge in a wide range of science and engineering fields including geotechnical, petroleum, mining, minerals, advanced materials and chemical engineering. Rocks have inherent granular arrangement and bonding at grain level (Burnley 2013). A common feature of a fractured rock is the discontinuity of fracture path within its structure induced by shear localisation (Burnley 2013). Fracture path within the sedimentary rock are identified by irregular interlocking pegs and sockets (de Andrade and Stylolites 2000). Mineral sorting of rock samples have shown compositional differences at the grain scale, identified by irregular interlocking pegs and sockets where insoluble minerals concentrate (de Andrade and Stylolites 2000). As a result, they display non-homogeneous material properties at bulk scale (Amadei 1983). Fracture in rock occurs along weaker stress planes (Park 2013). The grains are displaced in directions perpendicular to the least principal stress under external loading (Secor 1965; Nikitin and Odintsev 1999; van der Pluijm and Marshak 2004; Singhal and Gupta, 2010).

A major challenge in characterising the mechanical response of heterogeneous rock media and its links to mobilising bulk strength characteristics is the identification of strain (/stress) distribution in rocks especially when they are opaque. Existing strength measurements of rock media are done either at macro scale using bulk strength testing devices, or at micro scale using strain gauges though some whole field optical techniques such as speckle interferometry is useful (Razumovsky 2011). However, for using conventional strain gauges, it is not always

easy to pre-locate the weak positions of the strain (or stress) propagation paths in the rock samples (Lawn 1993). Furthermore, their outputs are limited to bulk data (Fairhurst and Hudson 1999), for example the results are averaged over several orders of grain size (gauge length). Ideally one would like to track the distribution of stresses and strains inside three-dimensional rock samples under mechanical loading, but the scientific community is still far away from accomplishing this task more easily. This could be responsible for the lack of accurate theories for defining the strength distribution in deformed complex materials. The relative displacement of the grains in them culminates into crack propagation under mechanical loading and accounting for such micro effects in predicting their bulk strength is not yet well established. Attempts to track the fracturing process by visualising whole-field strain or stress distribution patterns, and linking the grain-scale and micro scale measurements to the bulk scale strength characteristics of heterogeneous materials (Lawn 1993) are generally scarce in the literature. This aspect is addressed in the current work.

In order to measure the strain (/stress) at point scale methods such as photoelastic stress analysis have been reported in the past using strongly bonded optically sensitive birefringent disks mimicking the sandstone and provided some macro-parameters (Zang and Stephansson 2009). The residual strain field within sandstone grains was mimicked using birefringent material to represent naturally shaped quartz grains while epoxy was used to represent the bonding cement (Zang and Stephansson 2009). The quartz-cemented sandstone was simulated in such a way that the simulation results reproduce the elastic modulus of the grains and cement of the experimental sandstone samples. Other probing tools such as ultrasound tomography and X-ray computed tomography were useful to measure some mechanical (Appoloni and Fernandes 2007) and internal micro structural properties (Winkler 1983) of the grains respectively. Such properties could significantly influence on the macroscopic strength characteristics of rock

samples (Holt et al. 2005). However, stress (strain) measurements on real sandstone material are required at grain-scale to understand realistic micromechanical features, which is one of the ambitions of the current work.

On the computational front, a number of methods including finite element method (FEM) (Burnley 2013) and discrete element method (DEM) (Cundall and Strack 1979) have been used to understand the strength characteristics of rock samples. The interaction between contiguous particles could be governed by different ways, for example using the simple linear spring-dashpot models (Cundall and Strack 1979) and more complex theories of contact mechanics (Dvorkin and Nur 1996; Hossain et al. 2011). Though large scale sample representation in DEM is computationally expensive, some DEM studies have been reported for small scale rock samples (Hunt et al. 2003). However, DEM modelling fundamentally requires assigning initial values of different micro parameters (e.g. structural coordination number of the grains, porosity and stiffness parameters) of particle and inter-granular bond strength to build a rock sample. Usually such micro parameters are either guessed or obtained through a calibration processes in such a way that at first, the tuned parameters result bulk strength values of rock samples comparable with physical experiments using real samples (Yoon 2007). Thereafter, internal characteristics such as velocity and displacement patterns inside the samples at different stages of the loading could be probed in detail (Cundall and Strack 1979; Fakhimi and Villegas 2007). Experimental design and optimisation strategy have been reported to build discrete models which were subsequently used to calculate micro-parameters of grains in order to reproduce macro-properties (compressive strength, young's modulus and Poisson's ratio) of the rock during compression test (Yoon 2007). Some discrete models employ the technique of calibrated circular particle interaction to obtain a suitable dimensionless parameter for building granular rock models (Fakhimi and Villegas 2007) such that granular bond models are fine

tuned to suitable micro-properties (normal/shear stiffness, normal/shear bonds, and frictional coefficient) during the calibration procedure. Micro-properties were evaluated using a slightly overlapped circular particle interaction (SOCPI) (Fakhimi and Villegas 2004) to work out the ratio of the unconfined compressive strength to the tensile strength as well as the failure envelope. However, the resulting macroscopic strength was less in magnitude when compared to the real rock sample. Fakhimi and Villegas improved on the overlap technique (Fakhimi and Villegas 2004, 2007) using dimensional analysis to calibrate the particle assembly for the Pennsylvania blue sandstone. In this, the micro-properties resulted underestimates of the macro-properties of the real rock sample using theoretical contact models. Some theoretical and DEM modelling studies of rock materials (Shen et al. 2016) consider the stiffness ratio of the grains as analogues to the ratio between the bulk shear modulus and elastic modulus of the granular bonds. Although previous iterative approaches have provided new insights on the internal behaviour of rock samples under mechanical loading, it would be desirable at first to evaluate the grain-scale input parameters of advanced simulation tools such as DEM using experimental characterisation tools as much as possible, and then to use them to simulate their strength and dilation characteristics of rock samples in a more realistic manner using DEM. This has formed the motivation of the current research using sandstone as a test material.

2. Experiments and Modelling

Advanced computational methods commonly used for analysing the strength of materials such as DEM and FEM in engineering applications, depend on different material parameters as an input. For better predictions, the material input parameters need to be realistic as much as possible. In this study, apart from characterising the physical, chemical and mechanical properties of sandstone using a range of experiments at both single-grain and bulk scales,

experimental reflective photo stress analysis (PSA) (Antony 2015; Antony et al. 2017) is also used to visualise shear strain (ϵ) distribution on sandstone sample under mechanical loading. In PSA, the measurement of deviator strain (ϵ) levels as presented later, could be made at or greater than 2nm scale. Hence the method is ideally suited to understand on how stress propagation occurs at microscale on the surfaces of cementitious materials such as sandstone rock under external loading environments. Different experimentally characterised material parameters are used as input into the DEM modelling for simulating its bulk strength and dilation characteristics here.

Before detailing the different methods involved, the key steps of the present study are summarised progressively as follows: Chemical and physical analysis of the sandstone sample (obtained from Niger Delta) was performed to get grain-scale chemo-physical properties. A Chevron sandstone sample (V-notched, Fig.1) was applied with a birefringent uniform coating on its surface. The V-notched sample was subjected to axial line-loading across its thickness in stages. Using PSA and considering that the material is elastic, the whole-field shear strain (ϵ) distribution profile was tracked at suitable points close to the tip of the notch and where the optical response is maximum. Using this information and image analysis, the load-displacement of the grains along vertical and horizontal directions at the selected points are inferred for different loading increments. Assuming that the contiguous grains experience these inferred stress (σ) components along orthogonal directions, and using a well-known inter-granular model (methods section), the incremental force and displacement components were computed. From this, the optical anisotropy index K_o of the sandstone was obtained. Conventional ultrasound testing was done to obtain the stiffness ratio K of sandstone (which is due to the ultrasound wave responses in them along orthogonal directions). The experimentally measured stiffness ratio K is fed as an input parameter (rather than commonly assuming as

K=1, pertaining to an isotropic and homogeneous material) and using clumped-spheres to reflect the size and coordination number of the grains of sandstone. Discrete element modelling (DEM) is performed to simulate the bulk stress-strain relation and dilation for a cylindrical sample subjected to quasi-static uniaxial compression and tri-axial compression loading conditions (strain rate $\sim 2.5 \times 10^{-4}$ /s). Evolution of some internal parameters such as the velocity distribution of grains is also done to understand its discontinuities and the evolution of the fracture plane. Finally physical experiments were also done for the sandstone cylindrical samples (90mm height and 38mm diameter) pertaining to both the loading condition of the DEM simulations mentioned above to compare the bulk stress-strain relations and dilation, and a good level of agreement is obtained between the experimental and simulation results to validate the present approach, which links experimentally measured point-scale information to bulk scale strength characteristics of opaque complex materials, in this case sandstone. To substantiate this further, DEM simulations for the above said loading environments were also performed for the case of K=1 for the purpose of comparisons.

2.1.Methods

2.1.1 Experiments: The elemental composition of sandstone was performed using SEM and X-ray elemental mapping. The porosity and density measures of sandstone were done using the Saturation and Calliper Technique (Ulusay and Hudson 2005). The compressive strength and deviator stress of sandstone were measured for 5 samples each using the standard uniaxial and triaxial compression machines respectively (Fig.2). However we verified that due to the similar chemical and microstructural properties of the samples, the strength estimates were similar between the number of samples tested. The stiffness ratio K of the sandstone was evaluated using the conventional ultrasound method (Charalampidou et al. 2011; Aydin 2014) based on the standard test procedure of the International Society of Rock Mechanics (ISRM) (Ulusay

and Hudson 2007), and correlated with the optical anisotropy K_0 from the current PSA methodology as described below.

2.1.1.1 Photo-Stress Analysis (PSA)

For understanding the ability of the rock material to deform and distribute strain (/stress) at different directions under external loading environments, conventionally electrical strain gauge rosettes are used (Lawn 1993). The implication is that the strain measurements are averaged over the gauge lengths much longer than the size of the individual rock grains. Most recently, whole-field techniques such as digital image correlation is widely applied for axial strain measurements and strain localisation in rocks (Zhang et al. 2013). However, DIC does not directly measure the deviator strain at the point of interest, but it could be estimated from the displacement measurements of the artificial or natural speckle patterns on the samples. Acoustic emission (Baud et al. 2004), and its combination with DIC, ultrasound tomography and X-ray tomography (Charalampidou et al. 2010,2011) have been also applied to understand the role of bulk deviator stress and its links to the shear and compaction bands in sandstone. PSA is capable of measuring the deviator stress (/strain) to characterise stress anisotropy in materials directly when subjected to external loading (Dally and Riley 1991).

In PSA, there are two methodologies based on the type of optical polariscope used: (i) transmission type and (ii) reflection type. Details on the working methodologies of optical stress analysis can be found elsewhere (Dally and Riley 1991). In brief, both needs the material under study to possess the birefringent (polarisation) characteristics, i.e., at the point of interest, the material transmits out the incoming light with a delay, referred to as retardation of the light vector, along its principal optical axes. The level this retardation depends on the loading of the material experience. Stress-optic law (Dally and Riley 1991) is used to directly relate the retardation to the deviator strain (/stress) and the retardation is measured using a suitable

polariscope. The transmission type polariscope is suitable for materials that allows light to pass through. For opaque materials such as rock, a thin layer of suitable birefringent coating (usually polymeric coating of a known strain optic coefficient (Dally and Riley 1991)) could be applied on the surface of the geometry under study and the retardation at any point of interest is measured using the reflection type polariscope (Antony 2015; Antony et al. 2017, Fig.3). In the present study polymeric coating of uniform thickness 300 ± 20 microns with a strain optic coefficient 0.06 m/m/(m/m) , i.e., in the unit of retardation/thickness/strain is used. Grey-field reflection polariscope (Lesniak et al. 1997; Dally and Riley, 1991) is used to measure the retardation on the surface of the samples under loading. It is worth noting that the micro coating was well bonded to the sandstone and no peeling occurred during the experiments. This was also verified optically, i.e., (i) no optical retardation in the initial sample under no external load – thus confirming the absence of any shrinkage stresses in the measurement region of the coating and (ii) the optical anisotropy measurement made in the current study are done at low load levels in the current application. These steps help to minimise any errors in the deformation measurements of the membrane. In this, a circularly polarised light sweeps on the surface of the sample under loading (Fig.3). The out-coming light is elliptically polarised and bears the retardation (due to strain differences between orthogonal directions) at the point of interest. This information can be analysed further using an optical analyser (Fig.3) (Lesniak et al. 1997). It is worth noting that, in the experimental setup the light trigger, the optical elements and the processor are synchronised in space and time. This would help to increase the accuracy of the retardation measurements, as well as increase the speed of the measurements. More details of this can be found in the existing literature (e.g. Lesniak et al. 1997). Photo-stress experiments provide the relative difference of speed of the principal components of light (and their variation along any given direction), hence related to the deviator strain ($\epsilon_{11} - \epsilon_{22}$) and not sensitive to strains that are hydrostatic ($\epsilon_{11}=\epsilon_{22}$) (Dally and

Riley 1991). For interpreting optical anisotropy index K_o , the traces (slopes) of the grain scale force-retardation curve is used. Reflective photoelastic studies have helped to evaluate the individual principal strain components in materials under external loading with some simplifications (Caputo and Giudice 1983). Some photoelastic studies (Raghuwanshi and Parey 2015) considered that, for an uniaxial normal loading applied along the crack tip, the major principal stress is far greater than the minor principal stresses ($\sigma_{11} \gg \sigma_{22}$) in the direction of loading at regions close to the crack tip. This scenario is analogous to the current study along the normal direction of loading of the V-notch. However, due to the recent advancement in the optical stress analysis (Donne et al. 2008), we need not assume that the above said condition is applicable at all regions in front of the crack tip in bonded grains, rather the experiments could provide clues on where $\epsilon_{11} \gg \epsilon_{22}$ and vice-versa at grain-scale level by individually examining the distribution of γ_1 , γ_2 (Fig. 4) together with the distribution of principal strain directions dominantly both along and orthogonal to the direction of loading. This simplification is applied in the well-known strain (or stress)-optic law (Dally and Riley 1991) to obtain the stress increments in the orthogonal components σ_{11} and σ_{22} (or corresponding strain components). Furthermore, the direction of the major principal strain (/stress) components in the positive and negative regions pertaining to the vertical (\perp) and horizontal (\parallel) planes respectively as illustrated using the Mohr's circle in Fig.4 (Dally and Riley 1991). We observed that they were practically orthogonal to each other in the region of the investigation (identified close to the notch tip where the optical response of the material was strong, Fig.4). Hence by scanning this strain map, one could locate the optimum positions to track the respective increase in strain level for external loading increments. The area scanning function of the post-processing software was used to locate the points where the positive and negative strain levels were the maximum. Simultaneously, using the optical image analysis

software, the vertical and horizontal components of the retardation vector could be inferred for the above mentioned points of interest (ignoring the effect of the minor component), and used to estimate the optical anisotropy index K_0 . The granular stress (σ_{ij})-force (F_{ij})-fabric relation of cemented grains could be represented as (Mavko et al. 2009) $F_{ij} = \sigma_{ij}A/[C(1 - \phi)]$ in which C = co-ordination number of the grains (average value of sandstone used) and ϕ = porosity of sandstone. This relation has been used to infer the analogous intergranular force and to plot the corresponding force-retardation characteristics (Fig.5). In the current study, the notch angle (Fig.1) is kept as 50° to get a better opto-mechanical response of the V-notch sandstone samples. This is because, based on Infra-red thermography measurements, our earlier investigations on the grain-level temperature distribution in sandstone samples have shown maximum temperature concentration factor (TOC) (Antony et al. 2016) in the regions close to the notch tip for the notch angle of about 50° . The grain-level displacements occurred dominantly in the grains experiencing the maximum TOC.

2.1.2 Discrete Element Method (DEM): The method (Cundall and Strack 1979) models the interaction between contiguous cemented grains of sandstone under external loading as a dynamic process and the time step is advanced in small increments using an explicit finite difference scheme. The simulation parameters of the DEM sample of the Niger Delta sandstone were assigned based on physical experiments as much as possible. For example, the latest developments in X-ray tomography (Charalampidou et al. 2011) allow to measure the three-dimensional structure of the rock assemblies (including their pores) precisely. Accounting for such a precision in the DEM work is outside the current scope. Rather, we created the random assembly of the grains with the porosity (/packing density) and average co-ordination number of the grains pertaining to their experimental characterisation measures. The grains are represented as fused (cemented) spherical grains (Fig.6) with a given bond strength

accounting for their standard deviation by distributing it randomly to the grains (Table 1). The three stages of the loading illustrated in Fig.6 are as follows (Li and Fjær 2012); Stage1: This corresponds to the initial stages of the loading where the load level is low. Cementitious bond and spheres could sustain tension. Stage 2: For further increase in the load at this intermediate stage, the overlapped-grain tries to separate. The grains are still bonded. Stage3: At the verge of the grain separation. The grain contact is defined here by a linear spring-dashpot sphere model (Li et al. 2012) with a parallel bond strength (Shen et al. 2016) simulating the cementitious materials between the grains of sandstone (Holt et al. 2005; Cundall and Strack 1979; Hunt et al. 2003; Fakhimi and Villegas 2007; Shen et al. 2016), stiffness ratio of the springs and friction coefficient to govern the sliding of the grains. The stiffness ratio K of the sandstone was assigned in the DEM simulations corresponding to the evaluations using the conventional ultrasound method (Aydin 2014), and correlated with the current PSA methodology in the following section. The DEM simulations are performed primarily to assess the bulk strength measures such as the compressive and deviator strength (deviator stress) of sandstone subjected to the uni-axial compressive strength test and confined tri-axial strength test (Ulusay and Hudson 2007) under different levels of confining pressure. The outputs also include some information on the force distribution and velocity distribution of grains. However an extensive level of DEM analysis of strain localisation in sandstone (Charalampidou et al. 2011) is outside the scope of the current investigations.

3. Results and discussion

Figure 7 shows the SEM image of the Niger Delta sandstone sample and X-ray mapping of its elemental composition. This shows the granular nature and structure of the quartz grains which are cemented at their contacts in the sandstone. In sandstone, the bond strength of clay cementitious material is relatively weaker than the strength of quartz (Waltham 2001). The

coordination number of the quartz grains mostly varies between 8-12 (average coordination number 9) and the grain diameter between 60-100 microns. Furthermore, previous studies on the deformation of the grains in the rock have not rigorously accounted for the structural characteristics of the rock (Holt et al. 2005). However, considering that rock deformation is related to material properties at different scales, we obtain realistic information on the nature of strongly bonded grains in the sandstone sample studied here using the SEM and X-ray analysis. They suggest that the examined sandstone is composed of well-sorted quartz grains with random sizes (Fig.7). It is a clastic rock with low degree of heterogeneity. This is consistent with sedimentary oil-bearing rocks such as Niger Delta sandstone with random distribution of grain bonding; the grain morphology is multiplex (Lambert-Aikhionbare and Shaw 1982) with large pore space and low grain sphericity (Fig.7). Using the Saturation and Calliper Techniques (Ulusay R. & Hudson 2007), the following properties of the sandstone were measured: porosity 22%, grain density 2120 kg/m^3 and bulk density 2135 kg/m^3 . The friction coefficient of sandstone grains is obtained as 0.6 as normally assessed from the standard tri-axial test (Hoek and Franklin 1967) under a confined pressure of 15MPa, as an inter-granular experimental evaluation of this is complex to perform at this stage for bonded grains. The bond strength of sandstone grains is about 120-140MPa (Rong et al. 2013). Standard uni-axial and tri-axial confined compression test (Ulusay and Hudson 2007) of sandstone (Fig.2) were also conducted experimentally under a confining pressure of 15MPa, which resulted the values of the bulk compressive strength (failure strength), elastic modulus (E) and Poisson's ratio (ν) as 125MPa, 24.48GPa and 0.25 respectively. E and ν of the single grain-scale material is considered the same as that of the bulk material. The bulk compressive strength and deviator stress was also compared between the experiments and DEM simulation later. Experimental unconfined compressive strength test (Ulusay and Hudson 2007) of the sandstone was also conducted, which resulted the Young's modulus of sandstone as 18.6GPa.

This is within the range of other studies reported, for example 16.5GPa obtained experimentally for the Berea sandstone (Ord et al. 1991) and 20GPa used in the simulations for China sandstone (Rong et al. 2013).

The distribution of retardation of light between the major and minor optical axis on the V-notch sample (which is proportional to maximum shear strain (Dally and Riley 1991) is visualised using reflective PSA (Fig.3) for different axial load levels. Using the point-scale measurement of orthogonal stress (/strain) components, assuming that the point is represented by contiguous spheres in contacts using the sphere model (Li and Fjær 2012, Fig.6) and the approximation between stress-force at grain contact as used by Mavko (Mavko et al. 2009), the granular force can be inferred for different loading increments as presented in Fig.5. From this, the optical anisotropy index K_0 is inferred as 2.5. The standard deviation in K was ± 0.21 from a large number of repeated tests (about 50 samples). We also evaluated the stiffness ratio of the grains contact independently using the conventional ultrasound sensing methodology (Aydin 2014) which resulted the stiffness ratio $K = 2.5 \pm 0.18$. Based on this, K of sandstone is assigned as 2.5 in the DEM simulations, which is also comparable to K_0 characterised using PSA. It is worth pointing out that the K measured from the ultrasound method is based on the average response due to the contributions of all contacts in the experimental sample whereas the measurement of K_0 is point based. Henceforth, K is used as an input parameter into DEM modelling of the bulk strength of cylindrical sandstone sample at the later stage. Though not presented here, we had verified that the difference in results of DEM simulations by considering K_0 and K as the input of stiffness ratio was negligible. However further studies are required to establish the theoretical basis and exact correlations between K_0 and K for sandstone rock. Furthermore, it is interesting to note that existing DEM modelling studies on the strength characteristics of sandstone used the input value of K in the range 1.8-2.9 (Rong

et al. 2013, Tang et al. 2013, Wang 2014). However, unlike measuring K in the current research, most of the above mentioned DEM studies calibrated the value of K (trial and error) by matching the simulation response to the experimental bulk strength of sandstone. Also the optical output presented in Fig.5 result the individual values of k_1 and k_2 as 6MN/m and 2.4MN/m. This can be compared reasonably well with the values of normal and shear stiffness of sandstone reported earlier in the literature, for example 7.1MN/m and 2.9MN/m respectively for Berea sandstone tested using ultrasound sensor under a confining pressure of 17MPa (Winkler 1983). Further investigations are needed to reveal the precise relations between K_0 and K , which is outside the scope of the current paper. However, the significance of utilising the distribution of shear stress (τ/strain) on sandstone is emphasised further in Fig.8 for a typical sandstone V- notch sample under the vertical line loading (Fig.1) at the verge of its failure. In this, we observed that the path of propagation front of the maximum shear stress coincided well with the physical advancement of the major crack line. Hence the maximum shear stress (τ/strain) distribution (which can be visualised on the whole surface of sandstone) could be utilised well to probe the micromechanical properties of rock materials at both local and global scales in future. The input parameter used in the DEM simulations (including from the experimental characterisation results) are summarised in Table-1.

The DEM simulation results were compared with corresponding experimental tests as discussed earlier and the results are presented here. Furthermore, the simulation results for the case of sandstone if it were considered as an isotropic material (i.e., $K=1$) is provided for the purpose of comparisons. Figure 9a shows the variation of the unconfined bulk compressive strength (UCS) of sandstone. A good level of agreement is obtained from the simulation and experimental results, especially on the ultimate compressive strength of sandstone ($\sim 125\text{MPa}$). Furthermore, the dilation properties of the sandstone sample are also presented in Fig. 9(b)

from both the DEM simulations ($K=1, 2.5$) and experiments under the UCS test condition discussed earlier. It shows the variation of the volumetric strain together with the axial and lateral strain measured simultaneously using conventional electrical strain gauges (Lawn 1993) mounted on the experimental samples under different levels of axial stress levels. A good level of agreement is obtained between the results of the simulations using measured $K (=2.5)$ as input, and the experiments. Though the current study does not focus on other transport properties of sandstone, the dilation characteristics of rock samples are known to correlate to their permeability characteristics (Wang et al. 2016). The current modelling approach helps to obtain reliable measures of the dilation characteristics, hence enhancing its usefulness for such heterogeneous rock engineering research in future.

The shear behaviour (Timoshenko 1970) of the sandstone is also studied by plotting the variation of deviator stress (Timoshenko 1970, Towhata 2008) (i.e., the difference between the principal stresses) during the confined tri-axial test and presented in Fig.10 for typical cases of the confining pressure. Again, by and large the ultimate deviator stress levels of the samples agree well between the experimental and simulation results by using the measured stiffness ratio $K=2.5$. It is evident that, if we treat the sandstone as an isotropic materials (i.e., ignoring the measured grain-scale stiffness ratio of the sandstone and assuming $K=1$) the agreements between DEM results for the bulk compressive and deviator strength measures presented above do not agree with corresponding experimental bulk strength measures. This shows the usefulness of the current simulations in which measured grain-scale parameters, including the PSA measurement of stiffness ratio were utilised. However the variation of experimental bulk deviator stress showed some non-linearity in comparison with the experiments. Considering that the DEM simulations used a simple grain-scale constitutive behaviour here, the shear behaviour predicted from the simulations, mostly linearly until failure, is a fairly good average

representation of the corresponding experimental data. A detailed investigation on the DEM results of internal characteristics of sandstone including strain localisation could be reported in future. However, having validated the DEM simulations with experiments here, the variation of the resultant velocity of the grains obtained from the DEM simulations are presented in Fig.11. In this, the visual image of the failed sandstone sample is also inserted for the comparison. It is quite interesting to note that the failure plane of the experimental and simulation samples agree fairly well ($\sim 45^\circ$) and this further confirms the validity of the simulations and experiments reported in this research programme.

4. Conclusions

To conclude, the hybrid framework applied here and its validations gives a pathway for realistically simulating the multiscale behaviour of not only sandstone rock, but could be extended to other complex and heterogeneous engineering materials in linking their single grain-scale behaviour to the bulk mechanical properties in future. Furthermore, the current PSA approach could be combined with other experimental techniques such as thermography (sum of principal strains or stresses, Antony et al. 2016) in the samples under mechanical loading for a more accurate separation of strain components of the granular rock. Experimentally characterised input parameters of DEM simulations help to model the strength and dilation properties of complex materials such as sandstone using DEM more effectively. The current study provides useful information on the evolution of deviator stress (/strain) on sandstone using PSA. Combining this methodology with other experimental techniques such as AE, X-ray tomography and SEM could help to get a deeper understanding on the links between grain-scale properties, strain localisation and bulk mechanical properties of complex heterogeneous rocks as a multi-scale phenomena in future. Furthermore, the DEM simulations could be refined further by using varying stiffnesses of materials at the post-peak stages. This

could also help to capture the post-peak strength predictions of the experiments, for example to examine in detail the snap-back behaviour of some of the bulk compressive strength and bulk deviator stress results presented in the current work. Another possibility to improve the input to the DEM simulations is with regard to the approximation of considering the microscopic friction angle measured from the bulk friction test (using the bulk sample). However, measuring the microscopic friction for cementitious (/rock) materials in the true sense at grain scale is still not easy. Hence, in the present study, we had assumed it as same as from the bulk experimental test. It is shown here that K is shown to be more influential for the DEM simulations of sandstone than the effects of any potential difference between these two frictional values. This aspect needs further research to confirm.

REFERENCES

- Adeyanju, OA, Olafuyi, OA (2012) Experimental studies of sand production from unconsolidated sandstone petroleum reservoirs in Niger-delta. *Nijotech* 30, 18-30
- Amadei, B (1983) *Rock anisotropy and the theory of stress measurements*. Lecture notes in engineering 2, Springer-Verlag, New York
- Antony, SJ (2015) Imaging shear stress distribution and evaluating the stress concentration factor of the human eye. *Sci. Rep.* 5:8899
- Antony, SJ, Okeke, G, Tokgöz, D, Ozerkan, N (2017) Photonics and fracture toughness of heterogeneous composite materials. *Sci. Rep.* 7: 4539
- Antony, SJ, Olugbenga, A, Ozerkan, N, Marumoame, O, Okeke, G (2016) Sensing temperature and stress distributions on rock samples under mechanical loading. *ASCE Earth. Spa. Conf. Proc* 1570207489
- Appoloni, CR, Fernandes, CP, Rodrigues, CO (2007) X-ray microtomography study of a sandstone reservoir rock. *Nucl. Instrum. Meth.* 1:629-632
- Aydin, A (2014) Upgraded ISRM Suggested method for determining sound velocity by ultrasonic pulse transmission technique. *Rock Mech Rock Eng* 47:255-259

- Baud, P, Klein, E, Wong, T (2004) Compaction localisation in porous sandstones: spatial evolution of damage and acoustic emission activity. *Jl. Struc.Geol.* 26: 603-624
- Burnley, PC (2013) The importance of stress percolation patterns in rocks and other polycrystalline materials. *Nat. Commun.* 4:2117
- Caputo, F, Giudice, G (1983) Photoelastic coating method approach to the study of stress distribution in composite materials. *Fib. Sci.Tech.* 18:255-264
- Charalampidou, E-M, Hall, SA, Stanchits, S, Viggiani, G, Lewis, H (2010) Experimental characterization of shear and compaction band mechanisms in porous sandstone by a combination of AE and 3D-DIC. *EPJ Web.Conf.* 6:22009
- Charalampidou, E-M, Hall, SA, Stanchits, S, Lewis, H, Viggiani, G (2011) Characterization of shear and compaction bands in a porous sandstone deformed under triaxial compression. *Technophy.* 503: 8-17
- Cundall, PA, Strack, ODL (1979) A discrete numerical model for granular assemblies. *Geotechnique* 29:47-65
- Dally, JW, Riley, WF (1991) *Experimental Stress Analysis*, McGraw-Hill Inc, New York
- de Andrade, R, Stylolites, JR (2000): measurement of rock loss. *Braz. J. Geol* 30.3:432-435
- Donne, K et al (2008), Photoelastic stress and thermographic measurements of automotive windscreen defects generated by projectile impact. *Qual. Reliab. Engng. Int* 24:897–902
- Dvorkin, J, Nur, A (1996) Elasticity of high-porosity sandstones: Theory for two North Sea data sets. *Geophysics* 5:1363-1370
- Fairhurst, CE, Hudson, JA (1999) Draft ISRM suggested method for the complete stress-strain curve for intact rock in uniaxial compression. *Int. J. Rock Mech. Min. Sci.* 36:279-289
- Fakhimi, A, Villegas, T (2004) Calibration of a discrete element model for rock failure envelope and tensile strength. In Shimizu, Y, Cundall, P (eds.) *Numerical Modelling in Micromechanics via Particle Methods*, 383-390
- Fakhimi, A, Villegas, T (2007) Application of dimensional analysis in calibration of a discrete element model for rock deformation and fracture. *Rock Mech Rock Eng* 40:193–211
- Hoek, E, Franklin, JA (1967) *A simple triaxial cell for field or laboratory testing of rock*, ICST, University of London, London
- Holt, RM et al (2005) Comparison between controlled laboratory experiments and discrete particle simulations of the mechanical behaviour of rock. *Int. J. Rock Mech. Min. Sci.* 42:985–995

- Hossain, Z, Mukerji, T, Dvorkin, J, Fabricius, I.L (2011) Rock physics model of glauconitic greensand from the North Sea. *Geophysics* 6:E199-E209
- Hunt, SP, Meyers, AG, Louchnikov, V (2003) Modelling the Kaiser effect and deformation rate analysis in sandstone using the discrete element method. *Comput Geotech* 7:611-621
- Lambert-Aikhionbare, DO, Shaw, HF (1982) Significance of clays in the petroleum geology of the Niger Delta. *Clay Miner* 17:91-103
- Lawn, BR (1993) *Fracture of brittle solids*, Cambridge university press, Cambridge
- Lesniak, JR, Zickel, MJ, Welch, CS, Johnson, DF (1997) An innovative polariscope for photoelastic stress analysis. *Proc. SEM Spring conf. Exp. Mech.*, Bellevue, USA, 219-224
- Li, L, Fjær, E (2012) Modeling of stress-dependent static and dynamic moduli of weak sandstones. *J Geophys Res: Solid Earth* 117:WA103-WA112
- Mavko, G, Mukerji, T, Dvorkin, J (2009) *Tools for seismic analysis of porous media. The rock physics handbook*, Cambridge university press, Cambridge
- Nikitin, LV, Odintsev, VN (1999) A dilatancy model of tensile macrocracks in compressed rock. *Fatigue Fract Eng M.* 11:1003-1009
- Ord, A, Vardoulakis, I, Kajewski, R (1991) Shear band formation in Gosford sandstone. *Int. J. Rock Mech. Min. Sci.* 28:397-409
- Park, RG (2013) *Foundation of structural geology*, Routledge, Abingdon
- Raghuwanshi, N, Parey, A (2015) Mesh stiffness measurement of cracked spur gear by photoelasticity technique, *Measure* 73:439–452
- Razumovsky, IA (2011) *Interference-optical methods of solid mechanics*, Springer-Verlag, Berlin
- Ren, XH, Wang, HJ, Zhang, JX (2012). Numerical study of AE and DRA methods in sandstone and granite in orthogonal loading directions. *Water Sci. Eng* 5:93-104
- Rong, G, Liu, G, Hou, D, Zhou, CB (2013) Effect of particle shape on mechanical behaviors of rocks: A numerical study using clumped particle model. *Scientific World J*, 589215
- Secor, DT (1965) Role of fluid pressure in jointing. *Am. J. Sci* 8:633-646
- Shen, Z, Jiang, M and Thornton, C (2016) DEM simulation of bonded granular material. Part I: Contact model and application to cemented sand, *Compu. Geotec.* 75: 192–209
- Singhal, BS, Gupta, RP (2010) *Applied hydrogeology of fractured rocks*, Springer, Dordrecht

- Tang, CL, Hu, JC, Lin, ML, Yuan, RM, Cheng, CC (2013) The mechanism of the 1941 Tsaoling landslide, Taiwan: insight from a 2D discrete element simulation. *Environ. Earth Sci.* 70, 1005-1019
- Timoshenko, SP, Goodier, JN (1970) *Theory of Elasticity*, McGraw-Hill, New York
- Towhata, I (2008) Prediction of permanent displacement due to liquefaction. *Springer Series in Geomech Geoengg* 537-587, Berlin, Heidelberg
- Ulusay R., Hudson, J.A (2007). The complete ISRM suggested methods for rock characterization, testing and monitoring: *ISRM Commission on Testing Methods*, 1974-2006, ISRM Turkish National Group, Turkey
- van der Pluijm, BA, Marshak, S (2004) *Earth Structure*, Second Edition, W.W. Norton & Company Inc, London
- Waltham, T (2001) *Foundations of engineering geology*, CRC Press, London
- Wang, H, Xu, W, Jia, C, Cai, M, Meng, Q (2016) Experimental research on permeability evolution with microcrack development in sandstone under different fluid pressures. *J. Geotech. Geoenviron. Eng.* 142, 04016014
- Wang, S, et al (2014) Rock-arch instability characteristics of the sandstone plate under different loading conditions. *Adv. Mater Sci. Eng* 950870
- Winkler, KW (1983) Contact stiffness in granular porous materials: comparison between theory and experiment. *Geophys. Res.* 11:1073-1076
- Yoon, J (2007) Application of experimental design and optimization to PFC model calibration in uniaxial compression simulation. *Int. J. Rock Mech. Min. Sci.* 6: 871-889
- Zang, A, Stephansson, O (2009) *Stress Field of the Earth*, Springer-Netherlands, Netherlands
- Zhang, H, Huang, G, Song, H, Kang, Y (2013) Experimental characterization of strain localization in rock. *Geophys. J. Int.* 194:1554-1558

ACKNOWLEDGEMENT

This publication was made possible by NPRP grant # 6-1010-2-413 from the Qatar National Research Fund (a member of Qatar Foundation). The statements made herein are solely the responsibility of the authors. AO wishes to thank PTDF, Nigeria for supplying some of the sandstone samples.

Figure captions:

Figure 1: Schematic diagram of the V-notch sandstone sample subjected to an axial line-loading (quasi-static) across its thickness (all dimensions are in mm).

Figure 2: Experimental set ups: (a) uni-axial compression machine and (b) tri-axial compression machine, also with the facility of ultrasound sensing of the samples.

Figure 3: Basic optical elements of reflective PSA setup for sensing retardation of principal components of light and maximum shear stress distribution on the surface of sandstone under axial loading. The contours pertain to different order of the fringes.

Figure 4: (a) Illustrative diagram of strain (/stress) components using Mohr's circle and (b) A typical image (magnified) of maximum shear strain distribution in the V-notch sample under the external normal loading (in PSA camera micro strain unit for illustration purpose of the heterogeneous distribution of shear beneath the notch tip under loading). The red and blue regions depicts the corresponding strains: in the dominantly positive (\perp) and negative regions (\parallel) (default arrow seen in the image could be ignored).

Figure 5: (a) Typical evolution of retardation (nm) and deviator stress (MPa) of the sample for an increase in external load level P (presented in fractions of the ultimate load P_u). Such maps are generated for a number of incremental loads and the outputs are analysed to interpret k (methods section): (b) k_1 (c) k_2 (For the fit line of both plots, $R^2 > 0.95$. The data for the initial stages are only plotted here as the primary purpose is to get the slope of these variations).

Figure 6: (a) Illustration of a typical neighbouring grains. Later in the DEM simulations, the contiguous grains' contact is modelled using spheres with bond strength pertaining to the cementitious bond between the grains. The grains experience the loading broadly in three stages (stages 1-3) (b) basic grain elements used in the DEM simulations. Values shown within the brackets are the proportion of particles used in the simulation sample to achieve the required average coordination number and porosity of the initial sandstone assembly.

Figure 7: Scanning Electron Microscope (SEM) Image of Niger Delta sandstone. (a) Grain-scale image of sandstone (b) Map of elemental composition in the SEM image of sandstone

Figure 8: (a) The variation of maximum shear stress in the V-notch sandstone rock sample at the verge of failure load (b) for the same sample, the visual crack path is provided. We observed that the advancement of the major crack line (/crack path) coincided with the path of maximum shear stress propagation.

Figure 9: (a) Variation of the compressive strength of sandstone obtained from the UCS test (b) Variation of volumetric, axial and lateral strains of the sandstone during loading. In these plots, the DEM results for the cases of $K=1$ and 2.5 are compared with the experimental result.

Figure 10: Variation of the macroscopic deviator stress during the tri-axial loading under different levels of confining pressure: (a) 5MPa (b) 10MPa (c) 15MPa and (d) 20 MPa. In these plots, the DEM results for the case of $K=1$ and 2.5 are compared with corresponding experimental results.

Figure 11: Typical variation of the (a) resultant velocity of grains and plots are presented for a vertical section passing through the middle of the sample (front view): (i) initial state (ii-iii) intermediate states (iv) at the verge of failure (b) resultant displacement of the grains at different stages of loading (confining pressure 15MPa). However the maximum value of the resultant displacement is entered

below the respective images in metre. The thickness of the arrows is proportional to the magnitude of the respective measures and (c) a typical visual image of the experimental sample at failure. The failure plane is similar to that of displacement (/velocity) discontinuities in the simulation samples at the verge of failure ($\sim 45^\circ$).

Table caption

Table 1: Grain Contact parameters used in the DEM simulations to analyse the mechanical properties of Niger Delta sandstone

Table 1: Grain Contact parameters used in the DEM simulations to analyse the mechanical properties of Niger Delta sandstone

Bond normal strength, mean (MPa)	120
Bond normal strength, std. dev (MPa)	10
Bond shear strength, mean (MPa)	120
Bond shear strength, std. dev (MPa)	10
Grain contact stiffness ratio, k_n/k_s	2.5
Young's modulus (GPa)	18.6
Porosity	22%
Grain density kg/m^3	2120
Grain radius ratio, $R_{\text{max}}/R_{\text{min}}$	1.66
Friction coefficient	0.6
Average initial coordination number	9

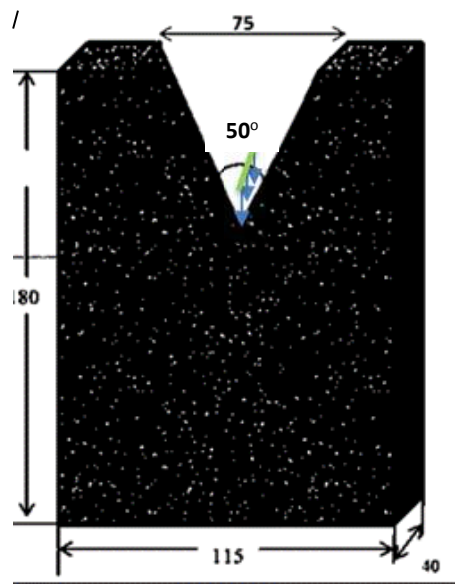
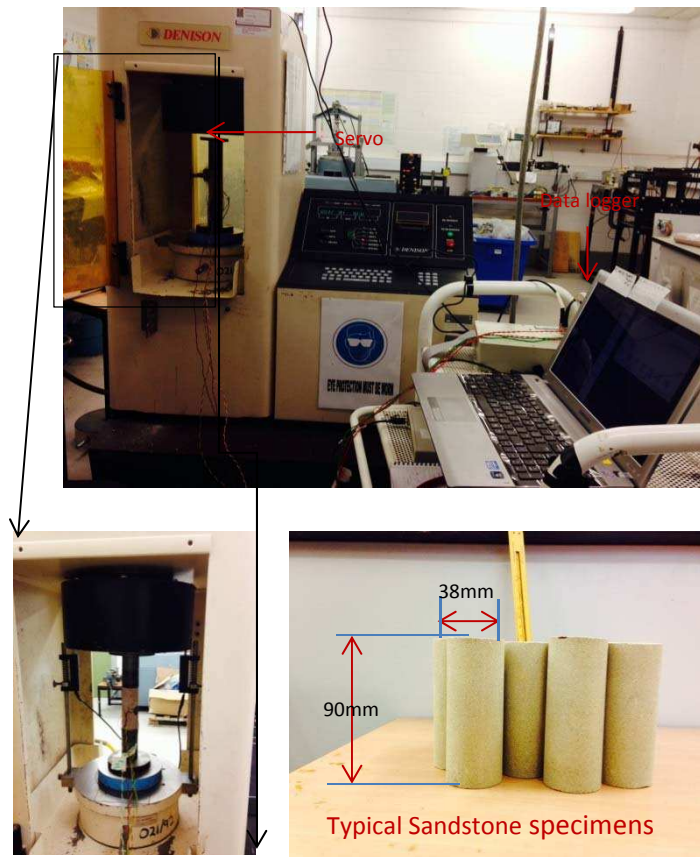
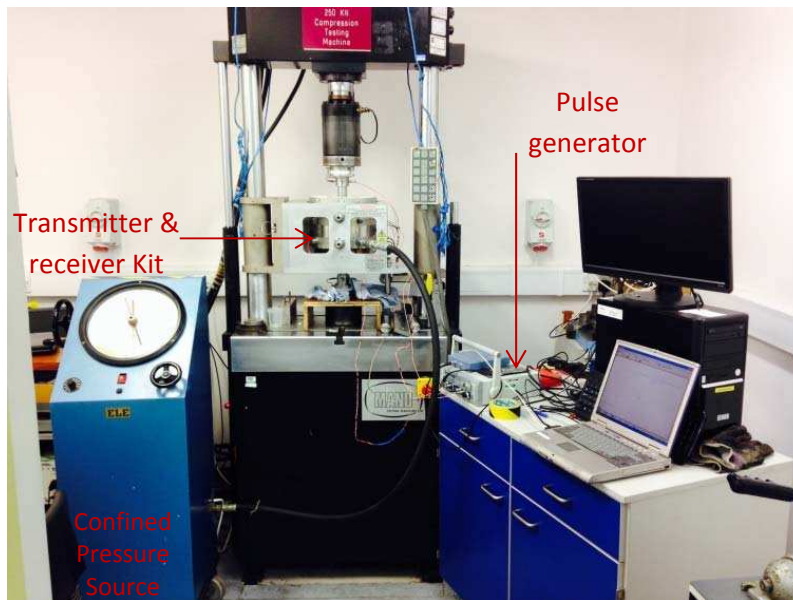


Figure 1: Schematic diagram of the V-notch sandstone sample subjected to an axial line-loading (quasi-static) across its thickness (all dimensions are in mm).



(a)



(b)

Figure 2: Experimental set ups: (a) uni-axial compression machine and (b) tri-axial compression machine, also with the facility of ultrasound sensing of the samples.

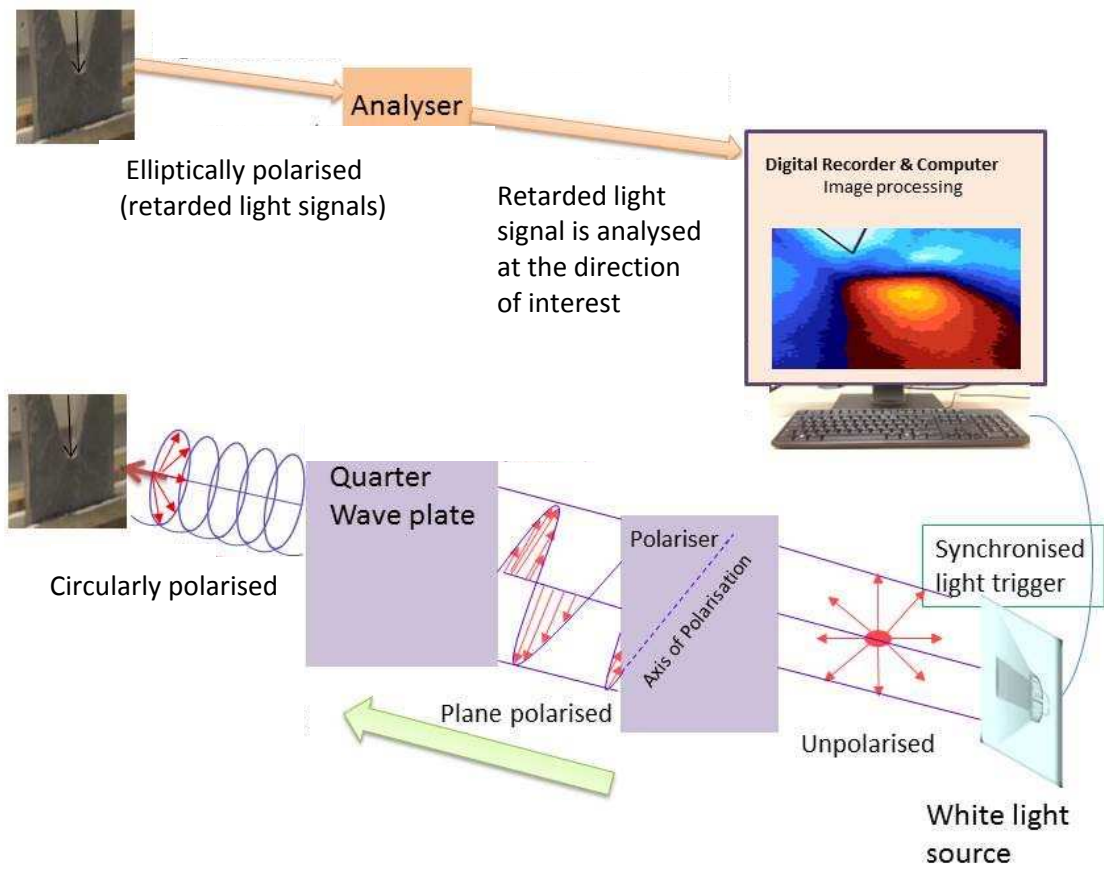
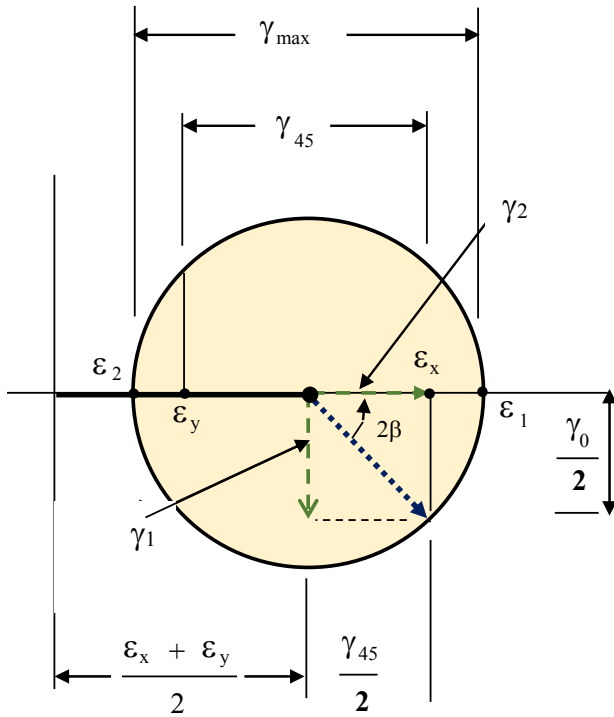
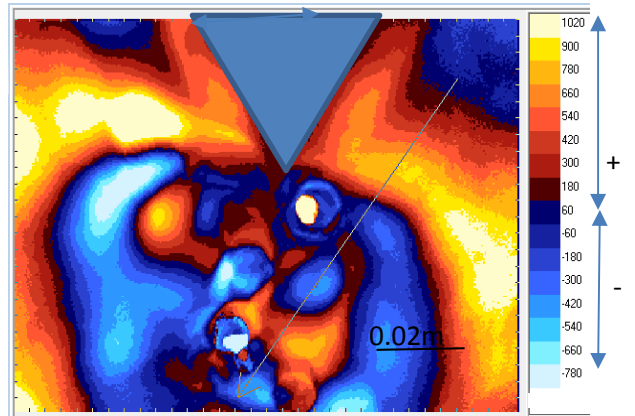


Figure 3: Basic optical elements of reflective PSA setup for sensing retardation of principal components of light and maximum shear stress distribution on the surface of sandstone under axial loading. The contours pertain to different order of the fringes.

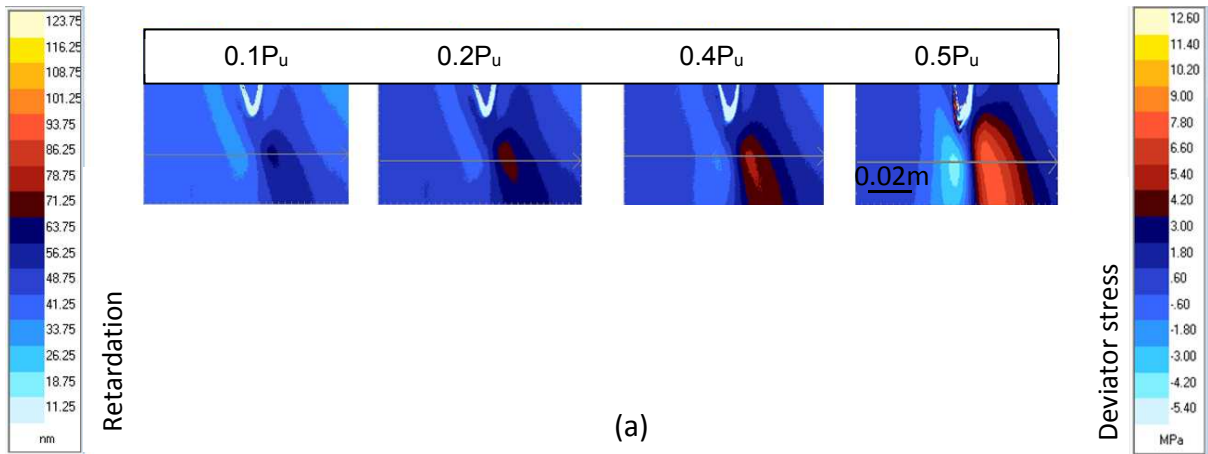


(a)

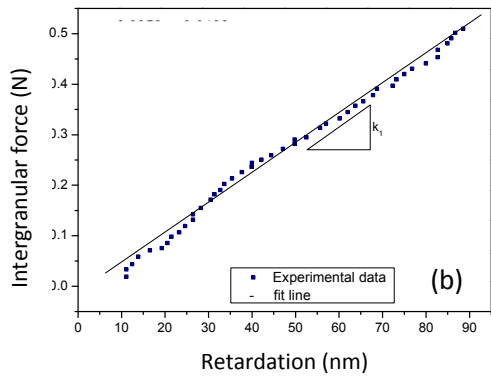


(b)

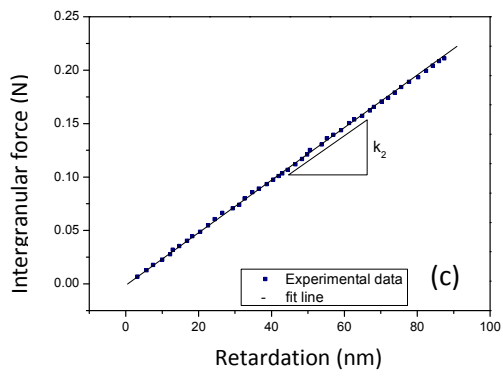
Figure 4: (a) Illustrative diagram of strain (/stress) components using Mohr's circle and (b) A typical image (magnified) of maximum shear strain distribution in the V-notch sample under the external normal loading (in PSA camera micro strain unit for illustration purpose of the heterogeneous distribution of shear beneath the notch tip under loading). The red and blue regions depicts the corresponding strains: in the dominantly positive (\perp) and negative regions (\parallel) (default arrow seen in the image could be ignored).



(a)



(b)



(c)

Figure 5: (a) Typical evolution of retardation (nm) and deviator stress (MPa) of the sample for an increase in external load level P (presented in fractions of the ultimate load P_u). Such maps are generated for a number of incremental loads and the outputs are analysed to interpret k (methods section): (b) k_1 (c) k_2 (For the fit line of the plots, $R^2 \approx 0.99$. The data for the initial stages are only plotted here as the primary purpose is to get the slope of these variations).

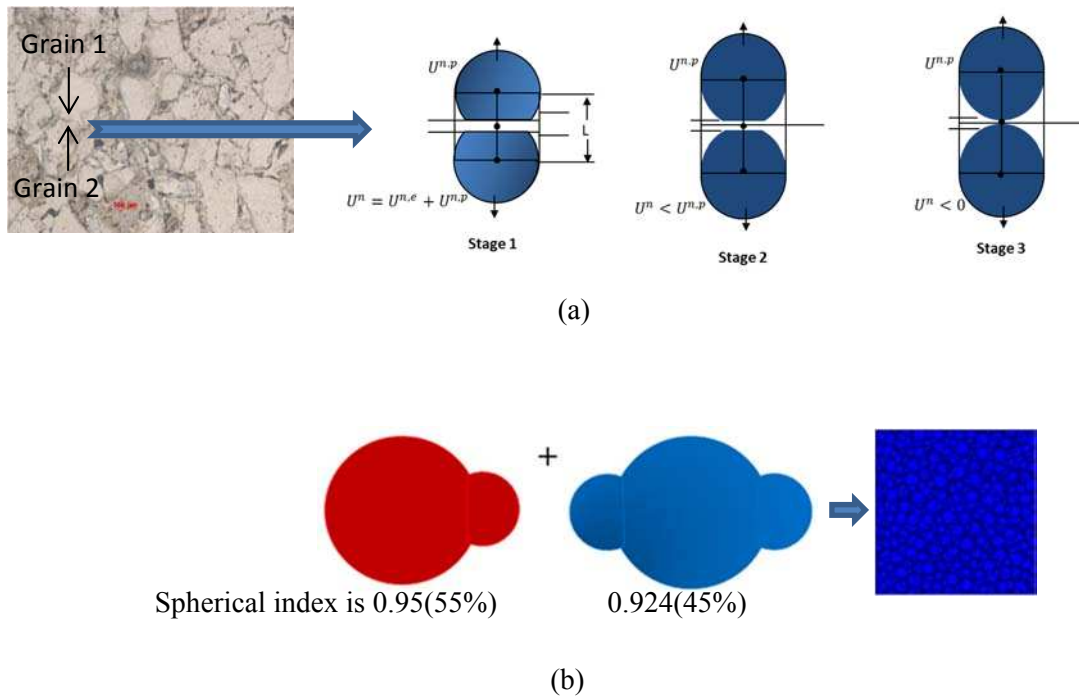
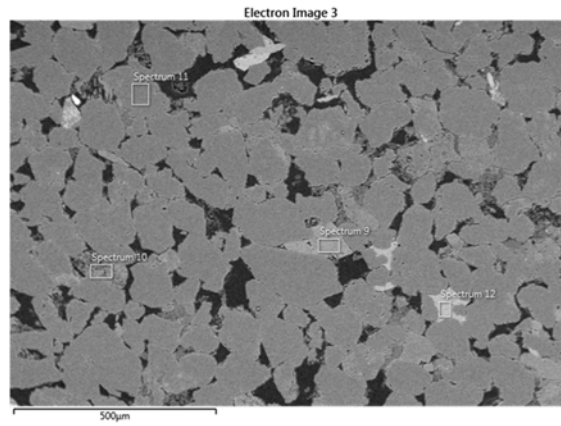
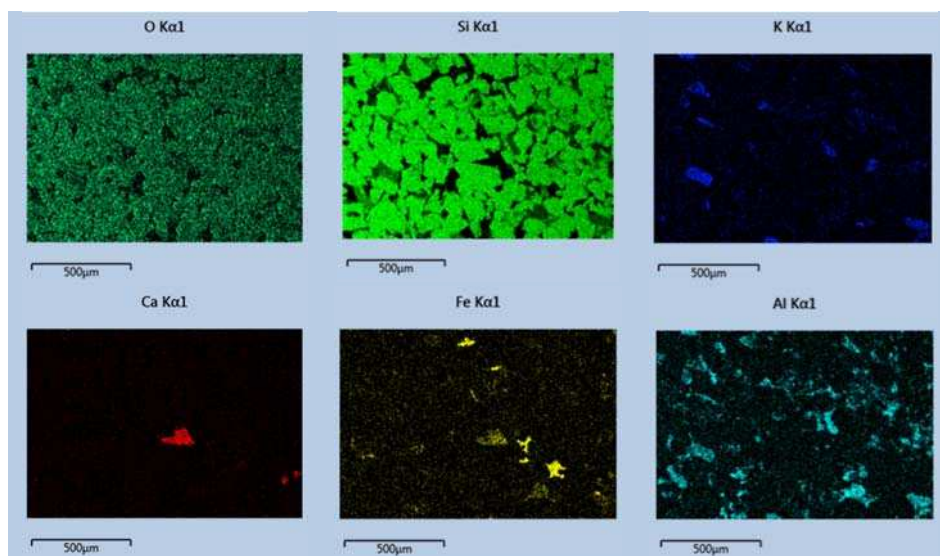


Figure 6: (a) Illustration of a typical neighbouring grains. Later in the DEM simulations, the contiguous grains' contact is modelled using spheres with bond strength pertaining to the cementitious bond between the grains. The grains experience the loading broadly in three stages (stages 1-3) (b) basic grain elements used in the DEM simulations. Values shown within the brackets are the proportion of particles used in the simulation sample to achieve the required average coordination number and porosity of the initial sandstone assembly.



(a)



(b)

Figure 7: Scanning Electron Microscope (SEM) Image of Niger Delta sandstone. (a) Grain-scale image of sandstone (b) Map of elemental composition in the SEM image of sandstone

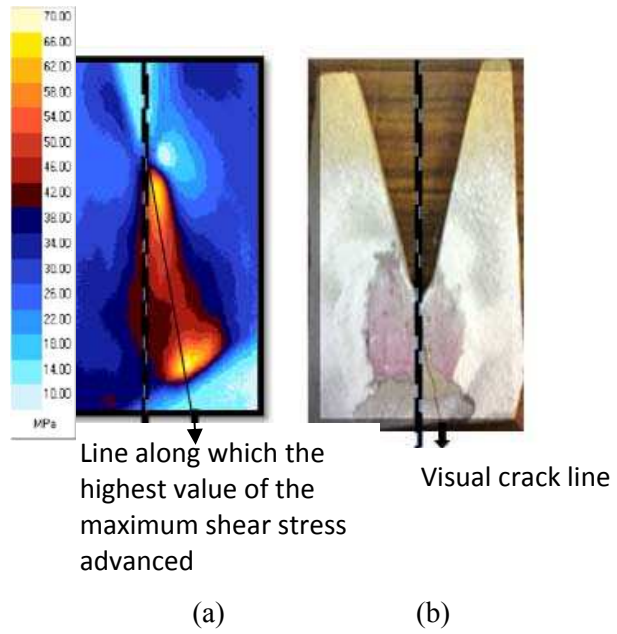


Figure 8: (a) The variation of maximum shear stress in the V-notch sandstone rock sample at the verge of failure load (b) for the same sample, the visual crack path is provided. We observed that the advancement of the major crack line (/crack path) coincided with the path of maximum shear stress propagation.

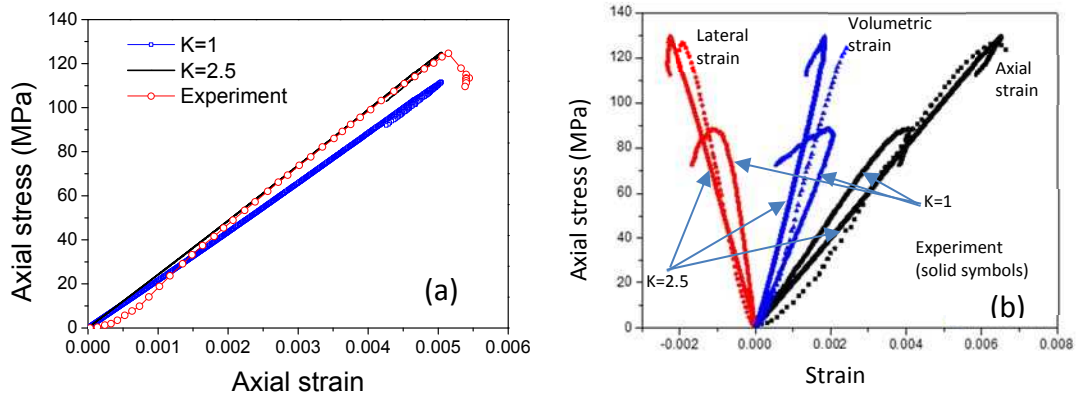


Figure 9: (a) Variation of the compressive strength of sandstone obtained from the UCS test (b) Variation of volumetric, axial and lateral strains of the sandstone during loading. In these plots, the DEM results for the cases of K=1 and 2.5 are compared with the experimental result.

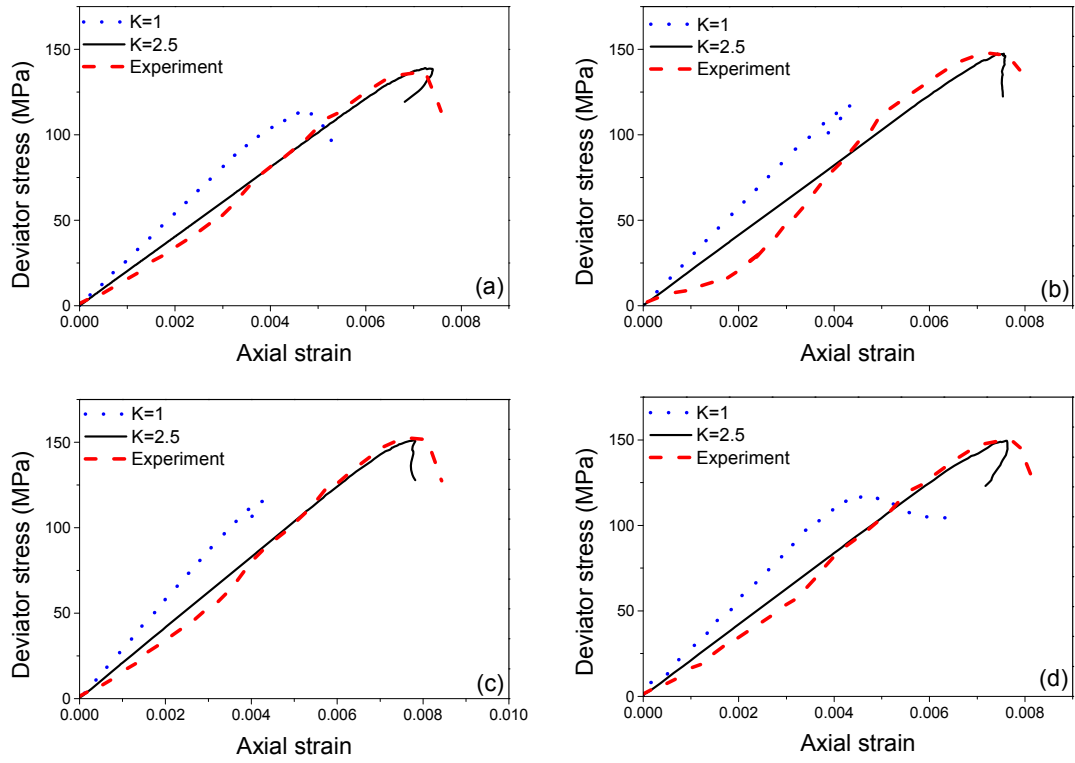


Figure 10: Variation of the macroscopic deviator stress during the tri-axial loading under different levels of confining pressure: (a) 5MPa (b) 10MPa (c) 15MPa and (d) 20 MPa. In these plots, the DEM results for the case of $K=1$ and 2.5 are compared with corresponding experimental results.

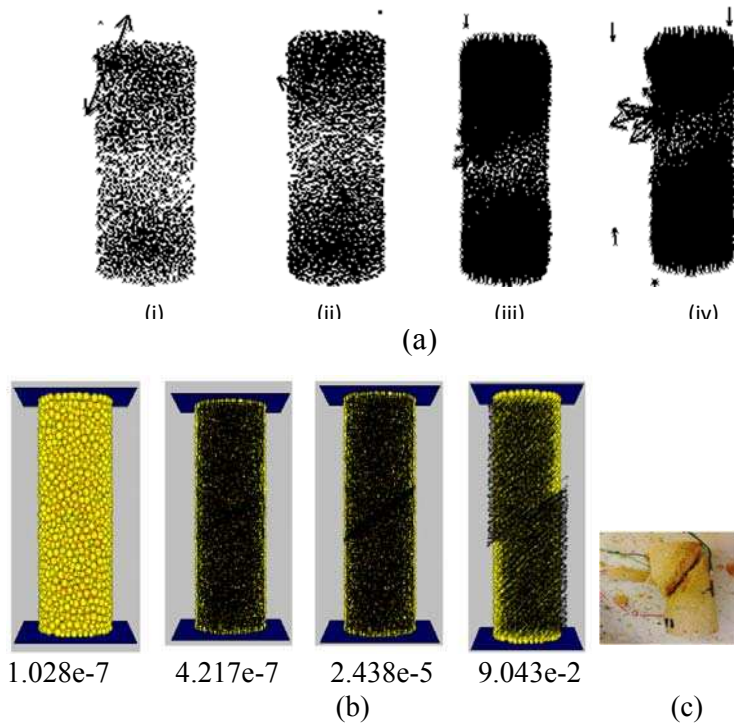


Figure 11: Typical variation of the (a) resultant velocity of grains and plots are presented for a vertical section passing through the middle of the sample (front view): (i) initial state (ii-iii) intermediate states (iv) at the verge of failure (b) resultant displacement of the grains at different stages of loading (confining pressure 15MPa). However the maximum value of the resultant displacement is entered below the respective images in metre. The thickness of the arrows is proportional to the magnitude of the respective measures and (c) a typical visual image of the experimental sample at failure. The failure plane is similar to that of displacement (/velocity) discontinuities in the simulation samples at the verge of failure ($\sim 45^\circ$).